



Article

Reaction Mechanism of CA_6 , Al_2O_3 and $\text{CA}_6\text{-Al}_2\text{O}_3$ Refractories with Refining Slag

Jie Liu ¹, Zheng Liu ², Jisheng Feng ³, Bin Li ^{1,*} , Junhong Chen ^{1,*}, Bo Ren ¹ , Yuanping Jia ³ and Shu Yin ^{4,5} 

¹ School of Materials Science and Engineering, University of Science and Technology Beijing, Beijing 100083, China

² Angang Construction Consortium Co., Ltd., Anshan 114001, China

³ Zibo City LuZhong Refractory Co., Ltd., Zibo 255000, China

⁴ Institute of Multidisciplinary Research for Advanced Materials, Tohoku University, 2-1-1Katahira, Aoba-ku, Sendai 980-8577, Japan

⁵ Advanced Institute for Materials Research (WPI-AIMR), Tohoku University, Katahira 2-1-1, Aoba-ku, Sendai 980-8577, Japan

* Correspondence: libin@ustb.edu.cn (B.L.); cjh2666@126.com (J.C.)

Abstract: In this study, to clarify the corrosion mechanism of CA_6 based refractory by refining slag, the static crucible tests for CA_6 , $\text{CA}_6\text{-Al}_2\text{O}_3$, and Al_2O_3 refractory, were carried out and the detail reaction processes were analyzed from the perspective of thermodynamic simulation and structural evolution. From the results, CaAl_4O_7 plays a vital role in the slag corrosion resistance of the three refractories. Regarding CA_6 refractory, the double pyramid module in CA_6 crystal structure was destroyed very quickly, leading to the rapid collapse of its structure to form the denser CaAl_4O_7 in high amounts. As a result, a reaction layer mainly composed of CaAl_4O_7 formed, which effectively inhibited the slag corrosion, so CA_6 refractory exhibits the most excellent slag corrosion. Meanwhile, the formation of CaAl_4O_7 can also avoid CA_6 particles entering the molten steel to introduce exogenous inclusions. For Al_2O_3 refractory, the generation of CaAl_4O_7 is much slower than that of CA_6 and $\text{CA}_6\text{-Al}_2\text{O}_3$ refractory, and the amount generated is also quite small, resulting in its worst slag corrosion among the three crucibles. Therefore, CA_6 based refractory has excellent application potential in ladle refining and clean steel smelting.

Keywords: corrosion resistance; refining slag; refractory; thermodynamic simulation



Citation: Liu, J.; Liu, Z.; Feng, J.; Li, B.; Chen, J.; Ren, B.; Jia, Y.; Yin, S. Reaction Mechanism of CA_6 , Al_2O_3 and $\text{CA}_6\text{-Al}_2\text{O}_3$ Refractories with Refining Slag. *Materials* **2022**, *15*, 6779. <https://doi.org/10.3390/ma15196779>

Academic Editor: Costica Bejinariu

Received: 30 August 2022

Accepted: 23 September 2022

Published: 30 September 2022

Publisher's Note: MDPI stays neutral with regard to jurisdictional claims in published maps and institutional affiliations.



Copyright: © 2022 by the authors. Licensee MDPI, Basel, Switzerland. This article is an open access article distributed under the terms and conditions of the Creative Commons Attribution (CC BY) license (<https://creativecommons.org/licenses/by/4.0/>).

1. Introduction

During the ladle refining process, the refractory is corroded severely due to the continuous reaction of the refining slag [1–3]. The slag corrosion will destroy the structure of the refractory and reduce the service life [4–7]. More importantly, under the continuous scouring effect of molten steel, the dislodged refractory and the corrosion products would enter the molten steel to form exogenous large size inclusions [8–17], which will have a fatally harmful effect on the purity of the molten steel and the quality of the final products [17–20]. Therefore, in order to eliminate the introduction of exogenous inclusion and to increase the service life of the refractories, it is absolutely essential to study corrosion behavior between the refractory and refining slag.

At present, the primary materials for the refining ladle are Al_2O_3 system refractories, due to their high density and stable high temperature properties. Many researches have been conducted to investigate the corrosion process between Al_2O_3 refractories and the refining slag [21–23], and many achievements have been obtained. It was found that the slag corrosion degree of Al_2O_3 refractories is influenced by factors such as temperature and refining slag composition [24–27]. Some scholars pointed out that [28,29] a small amount of $\text{CaAl}_{12}\text{O}_{19}$ generated on the surface of Al_2O_3 refractories can prevent further corrosion effectively, which is a critical mechanism. After years of development, an understanding of

the corrosion resistance of Al_2O_3 refractories has been profound, but there are few reports on the introduction and control of inclusions. So far, as Al_2O_3 refractories, the problem of introducing inclusions into molten steel is still unavoidable. With the development of cleanliness steel smelting, the effect of refractories on inclusions has attracted more and more attention. In order to prepare refractory materials with excellent corrosion resistance and less introduction of inclusions, in our previous work [30–34] we have synthesized the pure dense CA_6 (calcium hexaaluminate, $\text{CaAl}_{12}\text{O}_{19}$) base raw material and studied the slag corrosion resistance. After that, some researchers focused on optimizing CA_6 structure and tried to dope N^{3-} or Zr^{4+} into CA_6 [35,36], trying to improve performance further and achieve expected results. Besides that, from our recent experiments, the CA_6 -based refractories not only have excellent slag corrosion resistance but can also reduce the size of inclusions and absorb sulfur in steel. Researches on the preparation and structural improvement of CA_6 refractory are consummate. However, its slag corrosion mechanism is not clear, and the effect on the exogenous inclusion is not confirmed, which cannot provide strong support for promotion and application. Therefore, it is essential and meaningful to study the slag corrosion of CA_6 -based refractory, which has a great significance on refining ladle and even on the whole steelmaking process.

In this study, the reaction mechanism between two CA_6 -based refractory (pure CA_6 and CA_6 - Al_2O_3 composite) and refining slag was investigated and analyzed, and the Al_2O_3 refractory commonly used in the refining ladle was also used as a comparison. The microstructure and distribution of elements in the corrosion area were characterized, and the corrosion process was deduced and simulated by the thermodynamic software. The results of this work proved that CA_6 refractory has a great application prospect in the metallurgical industry due to excellent and distinctive slag corrosion resistance.

2. Materials and Methods

2.1. Preparation of the Crucibles and Refining Slag

The CA_6 , Al_2O_3 , and CA_6 - Al_2O_3 crucibles were prepared with CA_6 powder (purity > 98 wt%, particle size $\leq 74 \mu\text{m}$, Shengchuan, Shandong), Al_2O_3 powder (purity > 98 wt%, particle size $\leq 74 \mu\text{m}$, Shengchuan, Shandong), and the CA_6 and Al_2O_3 powder (mass ratio CA_6 : Al_2O_3 = 1:1), respectively. The static crucible method was adopted for the corrosion resistance test. Firstly, the dried powder was pressed under 30 MPa into $80 \times 80 \times 80 \text{ mm}^3$ cubes. Secondly, cylindrical holes with a diameter and height of 40 mm were drilled in the cubes as slag holes. Finally, the crucibles were fired at 1650 °C for 3 h. The properties of the crucibles are shown in Table 1.

Table 1. The properties of the crucibles.

Crucible	Bulk Density/(g/cm ³)	Apparent Porosity/(%)
CA_6	2.93	19.23
Al_2O_3	2.92	24.41
CA_6 - Al_2O_3	2.68	28.93

The chemical composition of the refining slag is shown in Table 2. The refining slag was prepared using analytically pure CaO (Sinopharm Chemical Reagent, purity > 99 wt%, particle size $\leq 74 \mu\text{m}$), Al_2O_3 (Sinopharm Chemical Reagent, purity > 99 wt%, particle size $\leq 74 \mu\text{m}$), MgO (Sinopharm Chemical Reagent, purity > 99 wt%, particle size $\leq 40 \mu\text{m}$) and SiO_2 (Sinopharm Chemical Reagent, purity > 99 wt%, particle size $\leq 74 \mu\text{m}$).

Table 2. Chemical compositions of the refining slag (wt%).

	CaO	Al_2O_3	MgO	SiO_2
Wt (%)	40	39	10	11

2.2. Experimental

The static crucible method was used to investigate the slag corrosion behavior of the three refractories. Put 70 g refining slag into the crucibles and then heat the crucibles to 1600 °C at a heating rate of 5 °C/min in the box furnace (KSL-1700X-M). After holding for 3h, the furnace stopped working and the crucible was taken out when it cooled to room temperature. The crucibles were cut along the center, and the corrosion area was made into a mosaic sample and then polished.

2.3. Characterization

The composition of the refining slag was analyzed by X-ray fluorescence spectrometry (XRF, Shimadzu, Japan). The micro-morphology of the slag-refractory interface was observed by scanning electron microscopy (SEM, FEI Nova nano 450, USA). The elemental distribution at the slag-resistant material interface was analyzed by SEM equipped with Energy Dispersive Spectrometer (EDS, EDAX Team, USA).

2.4. Thermodynamic Simulation

During the corrosion test, only the final result can be determined clearly and the intermediate process cannot be observed directly. Therefore, thermodynamic simulation for the slag corrosion process is necessary.

In this work, Factsage7.0 was used to simulate the corrosion process of three crucibles. The calculation mechanism is shown in Figure 1. The left side is refining slag and the right side is refractory, and the concentration of the refining slag and refractory at the interface area changes in the reverse cross between 0~1. During the calculations, the interface area is considered as a composition of multiple cross sections and the corrosion process of the refractory is simulated by predicting the generation of each section.

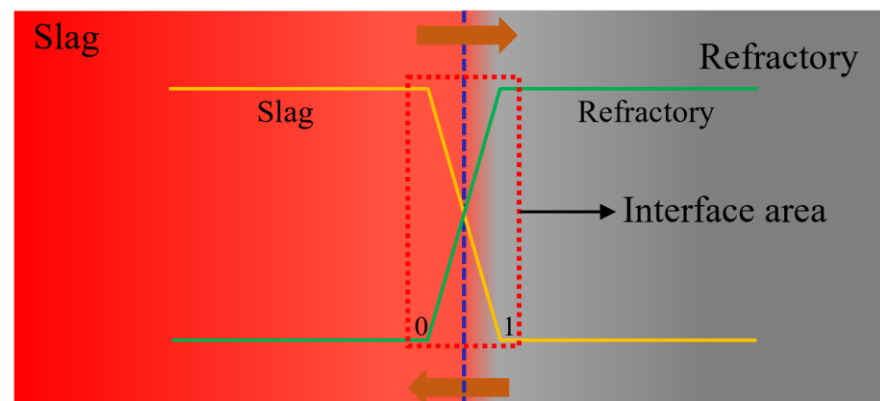


Figure 1. Thermodynamic calculation mechanism of the corrosion process.

The variable $\langle X \rangle$ in the Equilib module is used to calculate the inverse crossover interdiffusion, based on which to simulate the corrosion process of the refractory from thermodynamic aspect. When $X = 0$, the refining slag is all the composition of the system. When $x = 1$, the refractory is all the composition of the system. At the beginning of the reaction, X was defined as 1. With the decrease of X , more and more slag is involved in the reaction. The oxide data included in the calculation are available in the FToxid module. The calculated temperature was set at a constant 1873 k and the pressure was 1atm.

3. Results and Discussion

3.1. Composition Changes of Refining Slag

The composition of slag always changed due to the reaction with refractory. Figure 2 shows the variations of the refining slag composition after the corrosion test. As can be seen from Figure 2, the content of the CaO and MgO in the refining slag decreased, and the content of the Al₂O₃ increased in all three crucibles. It indicates that the CaO and MgO in

the slag reacted with or entered into the refractories, and Al_2O_3 in the refractories diffused into the slag during the corrosion process. The content of the SiO_2 in the slag remained almost unchanged, which is due to the large ionic radius of the silicate ion. The composition of the slag variation shows that the three crucibles were corroded by the refining slag in varying degrees.

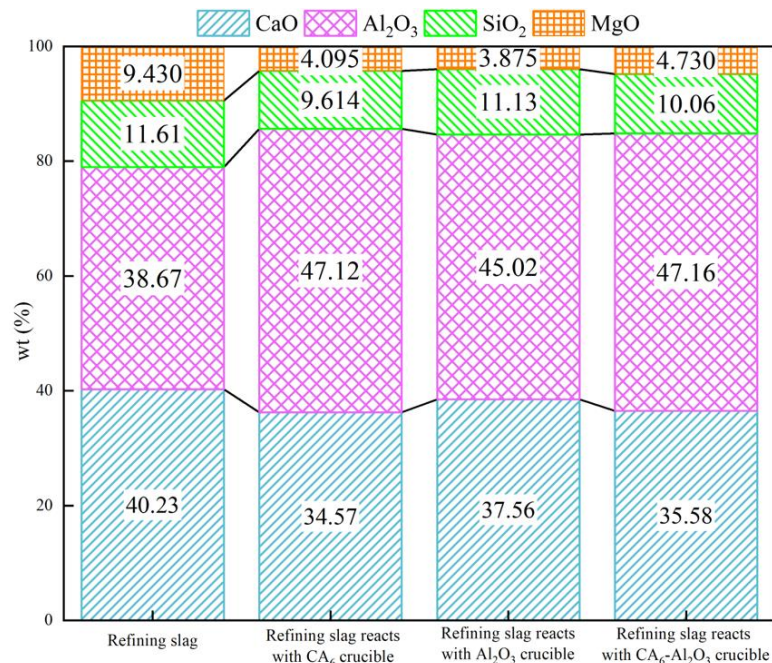


Figure 2. Composition variation of the refining slag.

3.2. Microstructure and Element Distribution

3.2.1. Corrosion of CA₆ Crucible

The microstructure results of the CA₆ crucible after slag corrosion are shown in Figure 3. The left side is the slag layer and the right side belongs to the original brick layer, and the reaction layer is in the middle, as shown in the red dotted area. It can be seen that many pores exist in the original brick layer. The average diameter of the pores ranged from 12 to 180 μm. In general, the higher porosity, the more severe corrosion of the crucible. However, the CA₆ crucible shows excellent slag resistance. At the slag-crucible interface, the width of the reaction layer is 50~60 μm, which is the thinnest of the three crucibles (Figures 5 and 7).

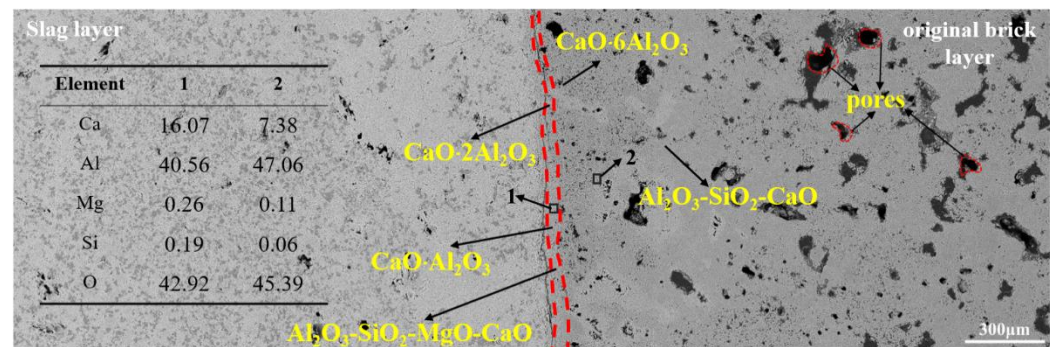


Figure 3. SEM image of CA₆ crucible after corrosion.

The EDS results show that CaAl_4O_7 generated at the slag-refractory interface (reaction layer), and most of the components in the reaction layer are CaAl_4O_7 (such as the EDS results of area 1). At the experimental temperature, liquid slag penetrated into the refractory through the pores and reacted with refractory to form CaAl_4O_7 , which is the

main reaction during the corrosion test. The corrosion of the refractory by the liquid slag was effectively inhibited due to the high viscosity of the CaAl_4O_7 . As the time increased, CaAl_4O_7 continued to react with CaO in the liquid slag to form CaAl_2O_4 in the reaction layer. In addition, a very small amount of slag phase of $\text{Al}_2\text{O}_3\text{-CaO-SiO}_2\text{-MgO}$ was found in the reaction layer. It can be clearly found that the microstructure of the reaction layer was denser than that of the original bricklayer. One of the reasons is the gaps and pores in the reaction layer were filled by CaAl_4O_7 and CaAl_2O_4 , which is also an important reason for preventing further corrosion of the refining slag. To reveal the penetration degree of the refining slag, area 2 was selected randomly for EDS analysis. The very limited Mg and Si were detected, indicating that the CaAl_4O_7 layer effectively prevents the penetration of the refining slag.

Figure 4 gives the element distribution result from the slag layer to the original brick layer. It can be seen that the amount of Al in the original brick layer is significantly more than that in the refining slag, while the amount of Ca was the opposite. Thus, it can be deduced that the Ca in the slag diffused into the refractory during the reaction, while Al diffused from the refractory to the refining slag. The amount of Mg and Si in the refractory was minimal, which can also be proved by the EDS result of area 2, indicating that only a very limited Mg and Si in the refining slag penetrate into the crucible through the pores or the gaps between grains.

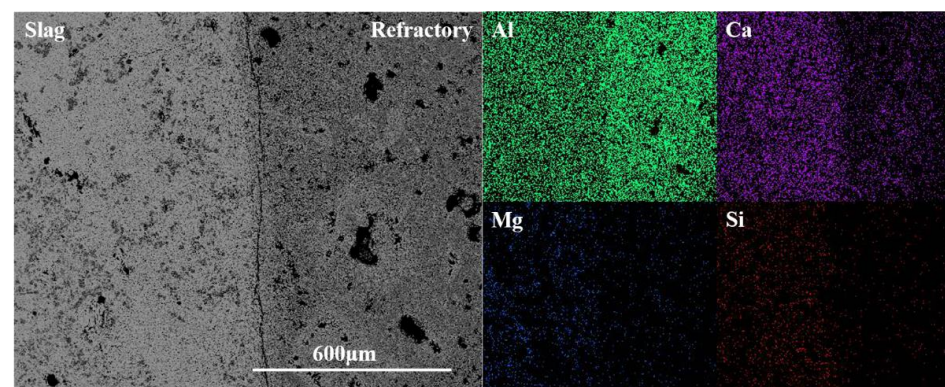


Figure 4. Element mapping of the slag-crucible interface of CA_6 crucible.

3.2.2. Corrosion of Al_2O_3 Crucible

Figure 5 exhibits the microstructure of the Al_2O_3 crucible after the static crucible test. As can be seen from Figure 5, from left to right are the slag layer, reaction layer, penetration layer, and original brick layer, respectively. The width of the reaction layer was $300\ \mu\text{m}$, and the maximum width of the penetration layer was more than $880\ \mu\text{m}$ that was the widest among the three crucibles.

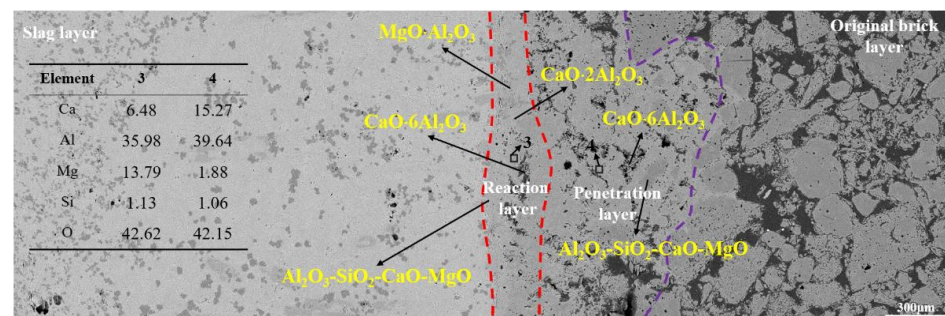


Figure 5. The SEM image of the Al_2O_3 crucible after corrosion by slag.

The EDS results show $\text{MgO}\cdot\text{Al}_2\text{O}_3$ generated in the reaction layer and it was formed by the reaction between MgO in the refining slag and Al_2O_3 in the refractory, which is the main component in the reaction layer. Some researchers [4,27] pointed out that the

presence of $\text{MgO}\cdot\text{Al}_2\text{O}_3$ at the interface has some hindrance to the penetration of slag. Meanwhile, trace amounts of CaAl_4O_7 were also detected in the reaction layer, but its generation mechanism is different from the CA_6 crucible. The Al_2O_3 in the refractory and CaO in the slag reacted to form $\text{CaAl}_{12}\text{O}_{19}$ first, and then the $\text{CaAl}_{12}\text{O}_{19}$ continued to react with CaO in the slag to form CaAl_4O_7 in the reaction layer. Compared with the CA_6 crucible, EDS results (area 3) show that the content of Mg in the reaction layer increased obviously and the amount of Ca decreased. It is confirmed again that the main phase was the $\text{MgO}\cdot\text{Al}_2\text{O}_3$ and the content of CaAl_4O_7 was limited in the reaction layer. Meanwhile, it can be noticed that the liquid slag phase was found in the reaction layer, and its content is more than that in the CA_6 crucible. In the penetration layer, except for the Al_2O_3 particles, the $\text{CaAl}_{12}\text{O}_{19}$ is also found in this area, proving that the Ca in the refining slag gradually penetrated into the refractory through the pores or cracks and reacted with the refractory. In addition, some of slag phase of $\text{Al}_2\text{O}_3\text{-CaO-SiO}_2\text{-MgO}$ was found in the penetration layer, proving that the reaction layer does not have an advantage in preventing slag penetration. The EDS results of area 4 show that the content of Mg and Si in the penetration layer is more than that of CA_6 and $\text{CA}_6\text{-Al}_2\text{O}_3$ crucibles, indicating the Al_2O_3 crucible has the worst slag corrosion resistance of the three crucibles.

Figure 6 is the element distribution result of the slag-crucible interface. It can be seen that the content of Al in the crucible was more than that in slag and Ca was detected in the slag at higher amounts. The element of Ca in the refractory mainly came from the penetration of the refining slag because of the absence of CaO in the raw material. A small amount of Mg and Si were found in the refractory, combined with the EDS result of area 4 in the penetration layer, which was most likely caused by the penetration of liquid slag.

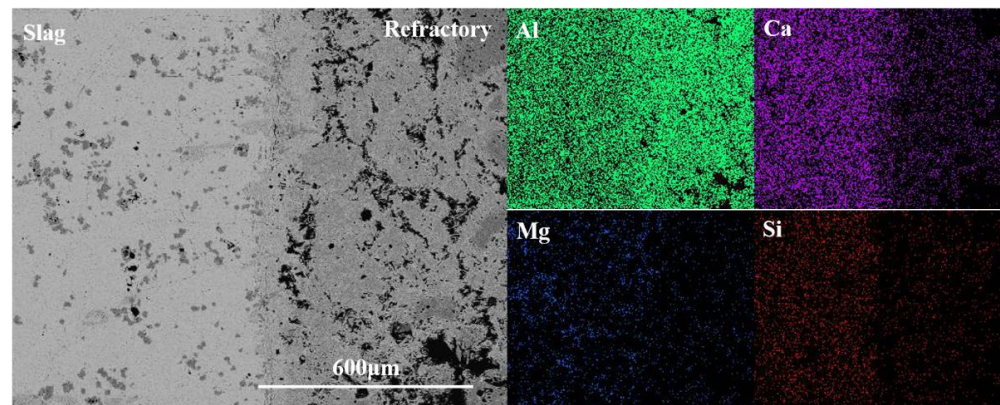


Figure 6. Element mapping of the slag-crucible interface of Al_2O_3 crucible.

3.2.3. Corrosion of $\text{CA}_6\text{-Al}_2\text{O}_3$ Crucible

Figure 7 shows the SEM image of the $\text{CA}_6\text{-Al}_2\text{O}_3$ crucible after the slag corrosion. From left to right are the slag layer, reaction layer, penetration layer, and original brick layer, respectively. From Figure 6, the reaction layer was generated between the refining slag and $\text{CA}_6\text{-Al}_2\text{O}_3$ crucible, and its width was about $200\ \mu\text{m}$, which was wider than that of the CA_6 crucible and thinner than that of the Al_2O_3 crucible. The microstructure of the reaction layer was denser compared to the original brick layer. In the reaction layer, CaAl_4O_7 is found from the EDS results, and it is quite possibly generated by the reaction between CA_6 in the refractory and CaO in the refining slag. Of course, a tiny part of CaAl_4O_7 may also come from the multistep reaction of Al_2O_3 in the refractory and CaO in the refining slag. In the CA_6 crucible, the CaAl_4O_7 can inhibit further corrosion of the refining slag. However, the content of CaAl_4O_7 in the $\text{CA}_6\text{-Al}_2\text{O}_3$ crucible was lower than that in the CA_6 crucible due to the limit of raw materials, which is one of the reasons for the wider reaction layer than that of the CA_6 crucible. In the reaction and penetration layer, a similar position to that of the CA_6 and Al_2O_3 crucibles was selected for EDS analysis. The results show the content of Ca in the reaction layer is less than that in the CA_6 crucible but more than in the

Al_2O_3 crucible, so it can be deduced that the amount of CaAl_4O_7 in the reaction layer is between the other two crucibles. In the penetration layer, the amount of Mg and Si was decreased compared with the Al_2O_3 crucible, indicating the slag corrosion resistance of the $\text{CA}_6\text{-Al}_2\text{O}_3$ crucible is better than the Al_2O_3 crucible but worse than the CA_6 crucible.

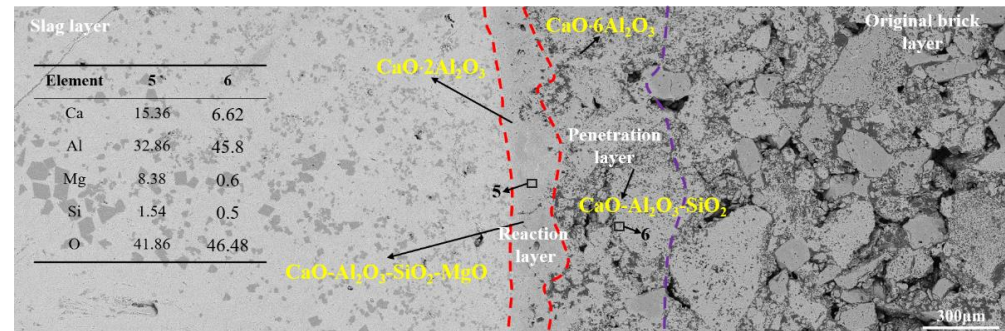


Figure 7. The results of the $\text{CA}_6\text{-Al}_2\text{O}_3$ crucible after corrosion by slag.

Figure 8 is the element distribution result of the $\text{CA}_6\text{-Al}_2\text{O}_3$ crucible. From Figure 8, the content of Al in the crucible was more than that in slag and Ca was detected in the refractory at higher amounts. The Mg and Si were also detected in the crucible and the content was less than that of the Al_2O_3 crucibles, which was also confirmed by the EDS result of area 6, proving the slag resistance of the $\text{CA}_6\text{-Al}_2\text{O}_3$ crucible was worse than the CA_6 crucible but better than Al_2O_3 crucible.

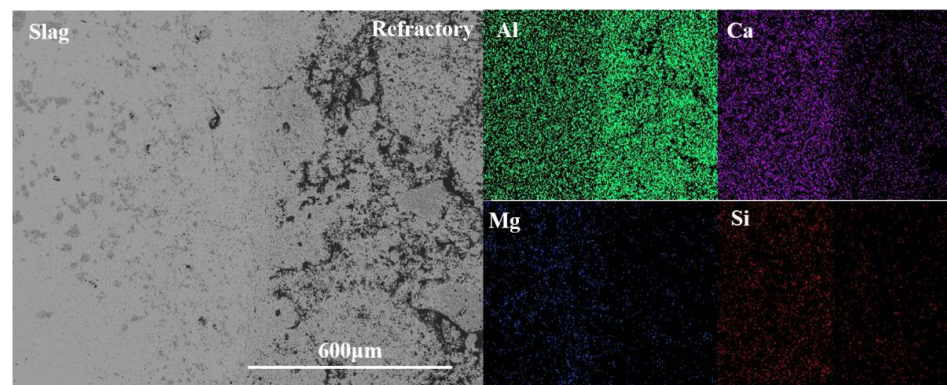


Figure 8. Element mapping of the slag-crucible interface of $\text{CA}_6\text{-Al}_2\text{O}_3$ crucible.

Through the above analysis, it can be found that the CA_6 crucible shows the best slag corrosion resistance, followed by the $\text{CA}_6\text{-Al}_2\text{O}_3$ crucible, and the Al_2O_3 crucible is the worst. The reaction mechanism of the CA_6 and Al_2O_3 crucible with the refining slag is shown in Figure 9. It can be seen from Figure 9a–c that the CA_6 particles reacted with the refining slag to form CaAl_4O_7 that can fill the pores or the gaps between the particles. Due to the high viscosity of CaAl_4O_7 , the slag-refractory interface will be denser and has a positive effect on inhibiting the slag corrosion. At the same time, it should be noticed that the probability of CA_6 particles entering the molten steel is greatly reduced due to the formation reaction layer, so the introduction of exogenous inclusions from the refractory is greatly reduced. In our recent work, it has been proved that the reaction product of the CA_6 refractory and refining slag can decrease the number and size of the inclusions. For the Al_2O_3 crucible, in addition to reacting with the Al_2O_3 particles at the interface, the refining slag also reacts with the inside Al_2O_3 crucible by penetrating into the refractory through the pores and the gaps between the Al_2O_3 particles, as shown in Figure 9d. During the corrosion process, the Al_2O_3 particles gradually dissolve or fall off into the refining slag, causing the more serious corrosion of the crucible, which is shown in Figure 9e,f. In addition, the fall-off particles can enter the molten steel and increase the number of inclusions in steel, which has a negative influence on the quality of steel production. Regarding the $\text{CA}_6\text{-Al}_2\text{O}_3$ crucible, the

CaAl_4O_7 is generated faster and the content is more due to the CA_6 raw materials compared with the Al_2O_3 crucible. Therefore, the slag corrosion resistance of the CA_6 - Al_2O_3 crucible is better than that of the Al_2O_3 crucible.

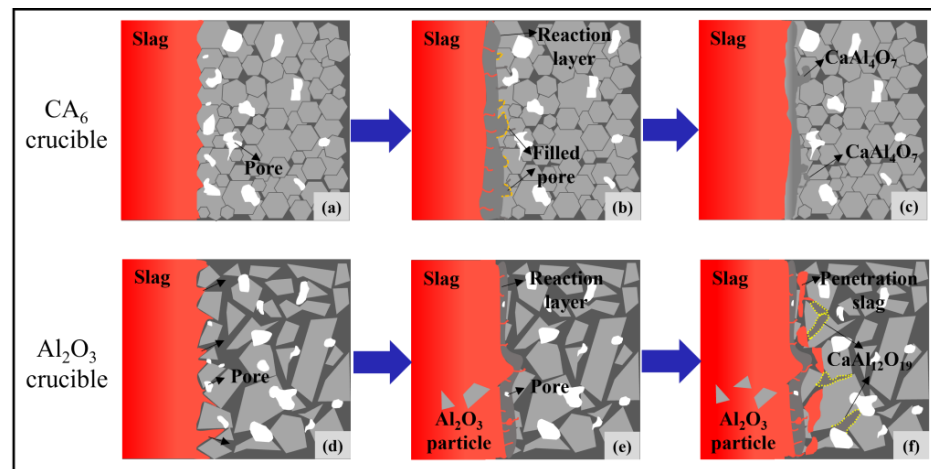


Figure 9. Reaction mechanism of the slag corrosion on the CA_6 and Al_2O_3 crucible. (a–e): The corrosion process of the CA_6 crucible; (d–f): The corrosion process of the Al_2O_3 crucible.

3.3. Thermodynamic Simulation of Corrosion of Crucibles by Refining Slag

The results of the thermodynamic simulation of the corrosion process of the CA_6 crucible are shown in Figure 10a. The corrosion process can be divided into the following steps according to the variation of X.

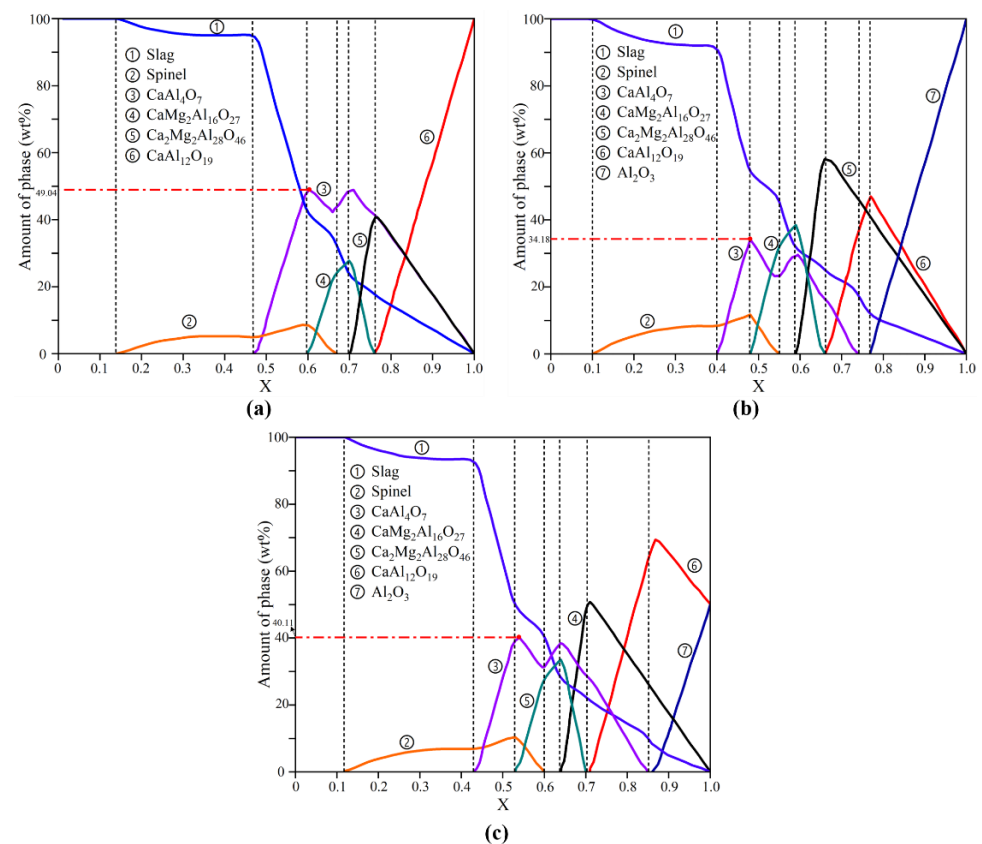
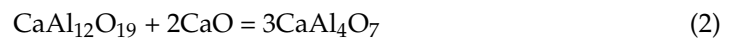
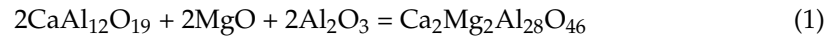
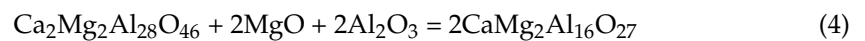


Figure 10. The thermodynamic simulation results of three crucibles: (a) CA_6 crucible, (b) Al_2O_3 crucible, and (c) CA_6 - Al_2O_3 crucible.

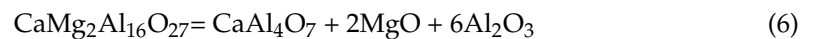
From Figure 10a, when $1.0 > X > 0.76$, four phases of CaAl_4O_7 , $\text{Ca}_2\text{Mg}_2\text{Al}_{28}\text{O}_{46}$, $\text{CaAl}_{12}\text{O}_{19}$, and liquid slag were obtained. With the decrease of X , the content of CaAl_4O_7 , $\text{Ca}_2\text{Mg}_2\text{Al}_{28}\text{O}_{46}$, and liquid slag increased while the content of $\text{CaAl}_{12}\text{O}_{19}$ decreased sharply. When $X = 0.76$, the content of $\text{Ca}_2\text{Mg}_2\text{Al}_{28}\text{O}_{46}$ reached a maximum of 40.95% and the content of $\text{CaAl}_{12}\text{O}_{19}$ was zero. $\text{Ca}_2\text{Mg}_2\text{Al}_{28}\text{O}_{46}$ and CaAl_4O_7 generated by the reaction of Equations (1) and (2):



When $0.76 > X > 0.7$, a new phase of $\text{CaMg}_2\text{Al}_{16}\text{O}_{27}$ appeared and increased with decreasing X while the content of $\text{Ca}_2\text{Mg}_2\text{Al}_{28}\text{O}_{46}$ gradually decreased until the content was zero at $X = 0.7$, indicating that $\text{Ca}_2\text{Mg}_2\text{Al}_{28}\text{O}_{46}$ gradually transformed into $\text{CaMg}_2\text{Al}_{16}\text{O}_{27}$ and CaAl_4O_7 following the Equations (3) and (4) respectively:

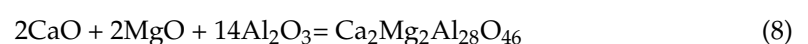


When $0.7 > X > 0.6$, the spinel phase appeared in the system at $X = 0.66$ through the reaction of Equation (5). The content of $\text{CaMg}_2\text{Al}_{16}\text{O}_{27}$ decreased gradually, and the content of CaAl_4O_7 increased gradually with the decrease of X , which indicated the $\text{CaMg}_2\text{Al}_{16}\text{O}_{27}$ continues to be converted to the CaAl_4O_7 by the equation (6). When $X = 0.6$, the content of $\text{CaMg}_2\text{Al}_{16}\text{O}_{27}$ was zero, while the content of CaAl_4O_7 and spinel reached the maximum content of 49.04% and 8.91%, respectively:



When $0.6 > X > 0.47$, the content of the CaAl_4O_7 decreased sharply and the liquid slag increased rapidly. When $X = 0.47$, the content of CaAl_4O_7 was zero. When $0.47 > X > 0.14$, two phases of liquid slag and spinel were in the system, and the content of spinel decreased to zero at $X = 0.14$. When $0.14 > X > 0$, the liquid slag was the only phase in the system.

The results of the thermodynamic simulation of the Al_2O_3 crucible and $\text{CA}_6\text{-Al}_2\text{O}_3$ crucible are shown in Figure 10b,c, respectively. The trends of the thermodynamic simulation results for the Al_2O_3 and $\text{CA}_6\text{-Al}_2\text{O}_3$ crucibles are roughly similar to the CA_6 crucible. However, significant differences existed in the beginning stage of the corrosion. For the Al_2O_3 crucible, when $1 > X > 0.76$, the Al_2O_3 converted to $\text{CaAl}_{12}\text{O}_{19}$ gradually by Equation (7), and the $\text{Ca}_2\text{Mg}_2\text{Al}_{28}\text{O}_{46}$ can also be generated through Equation (8). When $X = 0.76$, the phase of CaAl_4O_7 generated in the system and its content reached the maximum of 34.18% when $X = 0.48$, which is lower than that of the CA_6 and $\text{CA}_6\text{-Al}_2\text{O}_3$ crucible. For the $\text{CA}_6\text{-Al}_2\text{O}_3$ crucible, the Al_2O_3 converted to $\text{CaAl}_{12}\text{O}_{19}$ first, and then $\text{CaAl}_{12}\text{O}_{19}$ started to react with the refining slag to form CaAl_4O_7 at $X = 0.86$. And the maximum content of CaAl_4O_7 is 40.11% when $X = 0.54$, which is higher than that of the Al_2O_3 crucible but lower than that of the CA_6 crucible:



From the analysis of thermodynamic simulation, it can be found that the high melting point phase CaAl_4O_7 is the critical point in enhancing the slag resistance of the crucible [37–40]. The maximum content of the CaAl_4O_7 of the CA_6 , Al_2O_3 , and $\text{CA}_6\text{-Al}_2\text{O}_3$ crucible is 49.04%, 34.18%, and 40.11%, respectively, through the thermodynamic simulation results, which the trend is consistent with the EDS results. The CaAl_4O_7 was formed at the beginning of the reaction for the CA_6 crucible. For the Al_2O_3 and the $\text{CA}_6\text{-Al}_2\text{O}_3$ crucible, the CaAl_4O_7 was

formed at $X = 0.54$ and 0.86 , respectively. Therefore, the CaAl_4O_7 generated fastest and the amount was the most during the corrosion process of the CA_6 crucible, which had a great benefit on the slag resistance corrosion.

3.4. Crystal Structure Analysis of the Refractories

The results of the EDS analysis and thermodynamic simulations show that the CA_6 crucible can rapidly generate a higher amount of CaAl_4O_7 by reacting with the refining slag, while the Al_2O_3 crucible generates the CaAl_4O_7 through a series of reactions. In this section, the crystal structure of the CA_6 and Al_2O_3 is analyzed, and the reason for the difference in the CaAl_4O_7 generation rate and quantity between the CA_6 and Al_2O_3 is also explained.

Figure 11 shows the crystal structure of the CA_6 and Al_2O_3 . It can be seen that one Al and five O combined to form the double pyramid module in the mirror layer of the CA_6 crystal structure, as shown in the area circled red dotted line. The double pyramid module is the active site of CA_6 and is unstable during the reaction process. When the refining slag reacts with the crucible, the active site will be destroyed quickly, resulting in the rapid collapse of the CA_6 crystal structure to form the denser CaAl_4O_7 . The crystal structure of CaAl_4O_7 is more stable and can effectively inhibit the further corrosion of slag, which is one of the reasons for the excellent slag corrosion resistance of the CA_6 crucible. Al_2O_3 crystal is an octahedral structure and more stable compared to CA_6 , so the reaction rate with Ca in the refining slag is very slow, resulting in a low content of CaAl_4O_7 in the reaction layer and poor corrosion resistance. More importantly, Al_2O_3 particles with high stability may directly enter the refining slag and molten steel, resulting in the generation of exogenous inclusions, which has a negative impact on the control of inclusions. At this point, the CA_6 refractory can well avoid this problem. So, the excellent slag corrosion resistance of the CA_6 crucible has a great application prospect in the ladle refining process, especially for the smelting clean steel.

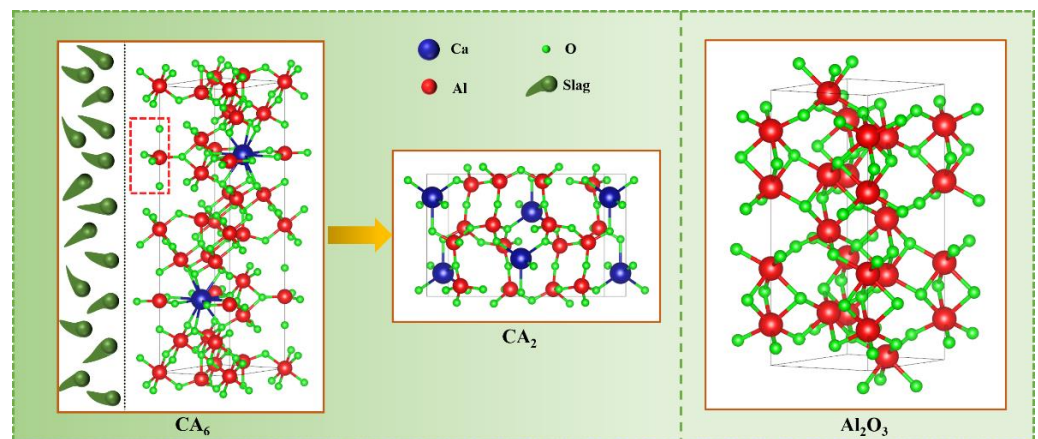


Figure 11. The crystal structure of CA_6 , CA_2 , and Al_2O_3 .

4. Conclusions

Three crucibles (CA_6 crucible, Al_2O_3 crucible, and CA_6 - Al_2O_3 crucible) were selected to investigate the corrosion resistance of the refining slag through laboratory experiments and thermodynamic simulations. The following conclusions were obtained.

(1) The three crucibles show different slag corrosion resistance, CA_6 crucible has the best corrosion resistance, followed by the CA_6 - Al_2O_3 crucible. The Al_2O_3 crucible shows the worst slag corrosion resistance.

(2) The addition of CA_6 to the raw materials has a positive effect on improving the slag corrosion resistance of the Al_2O_3 crucible.

(3) The generation of high melting point CaAl_4O_7 is the critical factor for inhibiting the further corrosion of the CA_6 and CA_6 - Al_2O_3 crucible. The CaAl_4O_7 was also detected in the Al_2O_3 crucible, but Al_2O_3 in the refractory reacts with CaO in the refining slag to produce

$\text{CaAl}_{12}\text{O}_{19}$ firstly, and then the $\text{CaAl}_{12}\text{O}_{19}$ reacted with slag to form CaAl_4O_7 . Therefore, the generation of CaAl_4O_7 in Al_2O_3 crucible is slower than that of CA_6 crucible and the amount generated is relatively less, which results in a worse slag corrosion resistance of Al_2O_3 crucible compared to CA_6 crucible and $\text{CA}_6\text{-Al}_2\text{O}_3$ crucible.

(4) When the refining slag reacts with the crucible, the double pyramid module of CA_6 will be destroyed quickly, resulting in the rapid collapse of the CA_6 crystal structure to form the denser CaAl_4O_7 , which is an essential reason for the excellent slag corrosion resistance. At the same time, it also avoids CA_6 particles entering the molten steel to introduce exogenous inclusions, so CA_6 has great application potential in ladle refining and clean steel smelting.

Author Contributions: Conceptualization, J.C. and S.Y.; methodology, B.L. and B.R.; writing and original draft preparation, J.L. and Z.L.; supervision and writing—review & editing, J.F. and Y.J. All authors have read and agreed to the published version of the manuscript.

Funding: This research was funded by National Nature Science Foundation of China, grant number 51874027, National Nature Science Foundation of China, grant number 51902018, and Major Science and Technology Innovation Project of Shandong Province, grant number 2019JZZY010359.

Institutional Review Board Statement: Not applicable.

Informed Consent Statement: Not applicable.

Data Availability Statement: Not applicable.

Conflicts of Interest: The authors declare no conflict of interest.

References

1. Chen, J.; Chen, L.; Wei, Y.; Li, N.; Zhang, S. Corrosion and penetration behaviors of slag/steel on the corroded interfaces of $\text{Al}_2\text{O}_3\text{-C}$ refractories: Role of Ti_3AlC_2 . *Corros. Sci.* **2018**, *143*, 166–176. [[CrossRef](#)]
2. Xu, L.; Chen, M.; Wang, N.; Yin, X.L. Corrosion mechanism of $\text{MgAl}_2\text{O}_4\text{-CaAl}_4\text{O}_7\text{-CaAl}_{12}\text{O}_{19}$ composite by steel ladle slag: Effect of additives. *J. Eur. Ceram. Soc.* **2017**, *37*, 2737–2746. [[CrossRef](#)]
3. Berjonneau, J.; Prigent, P.; Poirier, J. The development of a thermodynamic model for $\text{Al}_2\text{O}_3\text{-MgO}$ refractory castable corrosion by secondary metallurgy steel ladle slags. *Ceram. Int.* **2009**, *35*, 623–635. [[CrossRef](#)]
4. Riaz, S.; Mills, K.; Bain, K. Experimental examination of slag/refractory interface. *Ironmak. Steelmak.* **2022**, *29*, 107–113. [[CrossRef](#)]
5. Zou, Y.; Huang, A.; Gu, H. Novel phenomenon of quasi-volcanic corrosion on the alumina refractory-slag-air interface. *J. Am. Ceram. Soc.* **2020**, *103*, 6639–6649. [[CrossRef](#)]
6. Mills, K.C.; Su, Y.; Fox, A.B.; Li, Z.; Thackray, R.P.; Tsai, H. A review of slag splashing. *ISIJ Int.* **2005**, *45*, 619–633. [[CrossRef](#)]
7. Liu, C.; Huang, F.; Wang, X. The effect of refining slag and refractory on inclusion transformation in extra low oxygen steels. *Metall. Mater. Trans. B* **2016**, *47*, 999–1009. [[CrossRef](#)]
8. Huang, A.; Wang, Y.; Gu, H.; Zou, Y. Dynamic interaction of refractory and molten steel: Effect of alumina-magnesia castables on alloy steel cleanliness. *Ceram. Int.* **2018**, *44*, 22146–22153. [[CrossRef](#)]
9. Jones, P.T.; Vleugels, J.; Volders, I.; Blanpain, B.; van der Biest, O.; Wollants, P. A study of slag-infiltrated magnesia-chromite refractories using hybrid microwave heating. *J. Eur. Ceram. Soc.* **2002**, *22*, 903–916. [[CrossRef](#)]
10. Ali, M.; Sayet, T.; Gasser, A.; Blond, E. Transient Thermo-Mechanical Analysis of Steel Ladle Refractory Linings Using Mechanical Homogenization Approach. *Ceramics* **2020**, *3*, 171–189. [[CrossRef](#)]
11. Deng, Z.; Zhu, M.; Sichen, D. Effect of refractory on nonmetallic inclusions in Al-killed steel. *Metall. Mater. Trans. B* **2016**, *47*, 3158–3167. [[CrossRef](#)]
12. Deng, Z.; Cheng, L.; Chen, L.; Zhu, M. Effect of Refractory on Nonmetallic Inclusions in Si-Mn-Killed Steel. *Steel Res. Int.* **2019**, *90*, 1900268. [[CrossRef](#)]
13. Li, Y.; Yang, W.; Zhang, L. Formation mechanism of MgO containing inclusions in the molten steel refined in MgO refractory crucibles. *Metals* **2020**, *10*, 444. [[CrossRef](#)]
14. Beskow, K.; Tripathi, N.N.; Nzotta, M.; Sandberg, A.; Sichen, D. Impact of slag-refractory lining reactions on the formation of inclusions in steel. *Ironmak. Steelmak.* **2004**, *31*, 514–518. [[CrossRef](#)]
15. Brabie, V. Mechanism of reaction between refractory materials and aluminum deoxidised molten steel. *ISIJ Int.* **1996**, *36*, S109–S112. [[CrossRef](#)]
16. Shin, J.; Chung, Y.; Park, J. Refractory-Slag-Metal-Inclusion Multiphase Reactions Modeling Using Computational Thermodynamics: Kinetic Model for Prediction of Inclusion Evolution in Molten Steel. *Metall. Mater. Trans. B* **2016**, *48*, 46–59. [[CrossRef](#)]
17. Du, G.; Li, J.; Wang, Z. Effect of initial large-sized inclusion content on inclusion removal during electroslag remelting of H13 die steel. *Ironmak. Steelmak.* **2018**, *45*, 919–923. [[CrossRef](#)]

18. Lei, Z.; Hong, Y.; Xie, J.; Sun, C.; Zhao, A. Effects of inclusion size and location on very-high-cycle fatigue behavior for high strength steels. *Mater. Sci. Eng. A*. **2012**, *558*, 234–241. [[CrossRef](#)]
19. Holappa, L.; Helle, A. Inclusion control in high-performance steels. *J. Mater. Process. Technol.* **1995**, *53*, 177–186. [[CrossRef](#)]
20. Karr, U.; Sandaiji, Y.; Tanegashima, R.; Murakami, S.; Schoenbauer, B.; Fitzka, M.; Mayer, H. Inclusion initiated fracture in spring steel under axial and torsion very high cycle fatigue loading at different load ratios. *Int. J. Fatigue* **2020**, *134*, 105525. [[CrossRef](#)]
21. Zhang, S.; Rezaie, H.R.; Sarpoolaky, H.; Lee, W.E. Alumina dissolution into silicate slag. *J. Am. Ceram. Soc.* **2000**, *83*, 897–903. [[CrossRef](#)]
22. Choi, J.Y.; Lee, H.G.; Kim, J.S. Dissolution rate of Al₂O₃ into molten CaO-SiO₂-Al₂O₃ slags. *ISIJ Int.* **2002**, *42*, 852–860. [[CrossRef](#)]
23. Yan, P.; Webler, B.A.; Pistorius, P.C.; Fruehan, R.J. Nature of MgO and Al₂O₃ Dissolution in Metallurgical Slags. *Metall. Mater. Trans. B* **2015**, *46*, 2414–2418. [[CrossRef](#)]
24. de Bilbao, E.; Poirier, J.; Dombrowski, M. Corrosion of high alumina refractories by Al₂O₃-CaO slag: Thermodynamic and kinetic approaches. *Metall. Res. Technol.* **2015**, *112*, 607–621. [[CrossRef](#)]
25. Fernández, B.; Almanza, J.; Rodríguez, J.; Cortes, D.; Escobedo, J.; Gutiérrez, E. Corrosion mechanisms of Al₂O₃/MgAl₂O₄ by V₂O₅, NiO, Fe₂O₃ and vanadium slag. *Ceram. Int.* **2011**, *37*, 2973–2979. [[CrossRef](#)]
26. Song, J.; Liu, Y.; Lv, X.; You, Z. Corrosion Behavior of Al₂O₃ Substrate by SiO₂-MgO-FeO-CaO-Al₂O₃ Slag. *J. Mater. Res. Technol.* **2020**, *9*, 314–321. [[CrossRef](#)]
27. Tang, H.; Wu, G.; Wang, Y.; Li, J.; Lan, P.; Zhang, J. Comparative evaluation investigation of slag corrosion on Al₂O₃ and MgO-Al₂O₃ refractories via experiments and thermodynamic simulations. *Ceram. Int.* **2017**, *43*, 16502–16511. [[CrossRef](#)]
28. Wang, W.; Xue, L.; Zhang, T.; Zhou, L.; Chen, J.; Pan, Z. Thermodynamic corrosion behavior of Al₂O₃, ZrO₂ and MgO refractories in contact with high basicity refining slag. *Ceram. Int.* **2019**, *45*, 20664–20673. [[CrossRef](#)]
29. Fu, L.; Huang, A.; Gu, H.; Lu, D.; Lian, P. Effect of nano-alumina sol on the sintering properties and microstructure of microporous corundum. *Mater. Des.* **2016**, *89*, 21–26. [[CrossRef](#)]
30. Chen, J.; Yan, M.; Su, J.; Li, B.; Chou, K.C.; Hou, X.; Chen, M.; Zhao, B. Controllable Preparation of Al₂O₃-MgO-Al₂O₃-CaO-6Al₂O₃(AMC) Composite with Improved Slag Penetration Resistance. *Int. J. Appl. Ceram. Technol.* **2016**, *13*, 33–40. [[CrossRef](#)]
31. Li, B.; Li, G.; Chen, H.; Chen, J.; Hou, X.; Li, Y. Physical and mechanical properties of hot-press sintering ternary CM₂A₈ (CaMg₂Al₁₆O₂₇) and C₂M₂A₁₄ (Ca₂Mg₂Al₂₈O₄₆) ceramics. *J. Adv. Ceram.* **2018**, *7*, 229–236. [[CrossRef](#)]
32. Li, B.; Chen, H.; Chen, J.; Wang, E.; Hou, X.; Li, Y. Preparation, growth mechanism and slag resistance behavior of ternary Ca₂Mg₂Al₂₈O₄₆(C₂M₂A₁₄). *Int. J. Appl. Ceram. Technol.* **2019**, *16*, 1126–1137. [[CrossRef](#)]
33. Chen, J.; Chen, H.; Mi, W.; Cao, Z.; Li, B.; Liang, C.; Vance, L. Substitution of Ba for Ca in the Structure of CaAl₁₂O₁₉. *J. Am. Ceram. Soc.* **2017**, *100*, 413–418. [[CrossRef](#)]
34. Chen, J.; Chen, H.; Mi, W.; Cao, Z.; Li, B.; Li, G. Synthesis of CaO·2MgO·8Al₂O₃ (CM₂A₈) and its slag resistance mechanism. *J. Eur. Ceram. Soc.* **2017**, *37*, 1799–1804. [[CrossRef](#)]
35. Xu, L.; Wang, E.; Hou, X.; Chen, J.; He, Z.; Liang, T. Effect of incorporation of nitrogen on calcium hexaaluminate. *J. Eur. Ceram. Soc.* **2020**, *40*, 6155–6161. [[CrossRef](#)]
36. Guo, C.; Wang, E.; Hou, X.; Kang, J.; Yang, T.; Liang, T.; Bei, G. Preparation of Zr⁴⁺ doped calcium hexaaluminate with improved slag penetration resistance. *J. Am. Ceram. Soc.* **2021**, *104*, 4854–4866. [[CrossRef](#)]
37. Xiao, J.; Chen, J.; Li, Y.; Cheng, Y.; Nath, M.; Zhang, Y.; Zheng, L.; Wei, Y.; Zhang, S.; Li, N. Corrosion mechanism of cement-bonded Al₂O₃-MgAl₂O₄ pre-cast castables in contact with molten steel and slag. *Ceram. Int.* **2022**, *48*, 5168–5173. [[CrossRef](#)]
38. Darban, S.; Reynaert, C.; Ludwig, M.; Prorok, R.; Jastrzębska, I.; Szczerba, J. Corrosion of Alumina-Spinel Refractory by Secondary Metallurgical Slag Using Coating Corrosion Test. *Materials* **2022**, *15*, 3425. [[CrossRef](#)]
39. Wang, X.; Zhao, P.; Chen, J.; Zhao, H.; He, K. Corrosion resistance of Al-Cr-slag containing chromium-corundum refractories to slags with different basicity. *Ceram. Int.* **2018**, *44*, 12162–12168. [[CrossRef](#)]
40. Yin, H.; Gao, K.; Wan, Q.; Xin, Y.; Tang, Y.; Yuan, H. A comparative study on the slag resistance of dense corundum-spinel refractory and lightweight corundum-spinel refractory with density gradient. *Ceram. Int.* **2021**, *47*, 21310–21318. [[CrossRef](#)]